Light Management in Ultra-thin Conjugated Polymer Layers using Plasmonic Nanostructures for Optoelectronic Applications

by

Binxing Yu

A thesis submitted to the

Graduate School-New Brunswick

Rutgers, The State University of New Jersey

In partial fulfillment of the requirements

For the degree of

Master of Science

Graduate Program in Department of Chemistry & Chemical Biology

Written under the direction of

Prof. Deirdre O'Carroll

And approved by

_____

_____

_____

New Brunswick, New Jersey

Jan. 2016

ABSTRACT OF THE THESIS

Light Management in Ultra-thin Conjugated Polymer Layers using Plasmonic Nanostructures for Optoelectronic Applications

by

Binxing Yu

Thesis Director:
Deirdre O'Carroll

Plasmonics is a research area encompassing the fields of optics and nanoelectronics by confining light with relative large free-space wavelength to the nanometer scale. Specifically, plasmonic metal nanostructures have the potential to manage and enhance optical electromagnetic fields, making them essential tools for applications in fields such as photovoltaics, nano-optical sensors, enhanced information storage, light-emitting devices and photocatalysis. Also, the relatively high carrier transport rate, lower cost and synthetic tenability have given rise to an increasing amount of research on ultra-thin conjugated polymer films based optoelectronic devices, which indicates its essential role in next generation devices. Here, we demonstrate the deposition of gold monopole nanoantenna arrays onto sub-50 nm poly(3-hexylthiophene) (P3HT) films on Ag substrate can result in significant absorption enhancement (>12 at the P3HT band edge) and spectral

broadening (more than 250 nm increase) relative to P3HT/Ag films without plasmonic nanorod arrays. Full-field electromagnetic simulations are used to identify the modes of the plasmonic nanorod array/P3HT/Ag film system. In our case, gap modes are the primary contributor to the local field enhancement, hence the absorption enhancement in polythiophene thin film “gap” region. We then seek to validate the gap modes effect using single nanoparticle (NP) spectroscopy in the Ag NP/P3HT/Ag film system. Furthermore, future proposed work including photocurrent measurement through fabrication of ultra-thin nanoantenna incorporated organic photovoltaic devices, internal photoemission and light emitting diodes will be discussed.

Acknowledgement:

We acknowledge the financial support from the National Science Foundation (DMR-1309459), Institute for Advance Materials, Device and Nanotechnology and assistance from O'Carroll's group members.

Table of Contents

List of tables

List of illustrations

1. Introduction

One of the central challenges in organic thin-film optoelectronic devices is the achievement of effective, broadband light trapping and absorption (in the case of photovoltaic devices) and light out-coupling (in the case of light-emitting devices) in a sub-wavelength-thick active layers. Many approaches have been proposed to solve this issue such as surface texturing or the application of cavities or waveguides to the thin film to improve light management [1-7]. However, these methods are often limited by their micron-scale dimensions or by incompatibility with electrodes. However, with the widespread development of plasmonics, which is ultimately the control of the collective oscillatory motion of conduction electrons at a metal surface, light management in semiconductors has moved into a new era [8-18]. Essentially, plasmonics is a research area that merges the fields of optics and nanoelectronics by confining light with relatively large free-space wavelength to the nanometer scale, and because of this capability of subwavelength confinement, plasmonics forms the basis of the modern nanophotonics [12,13,18]. Plasmonic nanostructured metals (such as silver, gold, copper, aluminum) have been used in single molecule spectroscopy (SERS) [19,20], surface-enhanced Raman spectroscopy [21], solar cells [18], light emitting diodes [40] and catalysis [22].

These days, light scattering by the excitation of localized surface plasmons in metal nanoparticles has been used to demonstrate effective light trapping for photovoltaic applications [23-25]. Incorporation of plasmonic nanostructures in thin film solar cells could result in strong light confinement or trapping in the active layer because the plasmonic near-field around subwavelength metal nanoantennas is strongly coupled to the semiconductor which enables large scattering cross sections [18]. This property can lead to preferential scattering of the incident light into the semiconductor over an increased angular range, hence, enhancing the optical path length [26-33]. Therefore, optoelectronic devices incorporating plasmonic nanoantenna arrays can not only fully benefit from antenna near-field enhancement, but also from efficient light in-/out-coupling to sub-wavelength semiconductor material volumes. However, the detailed working mechanism of nanoantenna/semiconductor light management in terms of how incident light couples to a single nanoantenna, and the shape, type and degree of electromagnetic field localization of the plasmonic modes still requires further optimization. Additionally, the electronic properties of nanoantennas placed on or near electrical contacts, and the direct use of nanoantennas as electrodes for application to optoelectronic devices need further investigation [12].

Recently, a number of studies have begun to elucidate the mode structure and local field confinement that occurs between closely-spaced metallic nanoparticle/film

monopole nanoantenna systems [34,35]. Both gap and dipole/multipole modes have been identified and the mode properties depend on the distance between the metal nanoparticle and the underlying metal film, and on the size of the metal nanoparticle, respectively. Both mode types could be used to modify the properties of molecules or semiconductor “spacer” layers placed between the metal nanoparticle and the underlying metal film. Gap mode resonances, which can occur in narrow gaps between nanostructured metal surfaces, such as nanoparticle dimers, or when bringing a nanoparticle close to a metal surface, under normal incidence excitation, can lead to record levels of field amplification (up to factors of 10^{10}) [35,36]. These modes are extensively used in SERS and are of tremendous value in single-molecule, single particle detection [36,37]. However, research on gap mode resonances often consists of fundamental optical studies [32,41], and gap modes have rarely been applied to optoelectronic devices , possibly due to the challenge of forming ultra-thin semiconductor films that could be placed within gap mode regions. Our lab has recently fabricated an Au nanorod array/ultra-thin conjugated polymer layer/Ag film system that may be more amenable to electrical injection/collection schemes and investigated the influence of the system on the optical properties of the ultra-thin conjugated polymer layer. Additionally, we theoretically confirmed the significant contribution from gap modes to absorption enhancement in the conjugated polymer

active layer because electric fields were predominantly localized in that region [38,39]. However, experimental validation and further identification of how the gap mode wavelength, intensity and degree of localization can be optimized by changing factors such as: gap thickness; nanoparticle size/shape; or material type is still needed. Here, we seek to investigate single nanoparticle gap mode resonances characterized by dark-field spectroscopy for a Ag NP/P3HT/Ag film system in combination with scanning electron microscopy (SEM) and atomic force microscopy (AFM) to determine the physical parameters of the system.

2. Results to-Date

2.1. Light Management in Ultra-thin Conjugated Polymer Films using Vertically Oriented Nanoantenna Arrays

The large local density of optical states in the near-field of resonant plasmonic nanoantennas has been proved to significantly increase the efficiency of semiconductor absorption and emission processes. Additionally, the ability of plasmonic nanoantennas to localize light at sub-wavelength dimensions is synergistic with the application of ultra-thin film semiconductor layers to photodetection, solar energy harvesting and light-emitting devices [4-7]. Here, a monopole

nanoantennas/polythiophene/Ag film system has been designed and fabricated to enhance optical properties of ultra-thin (20 - 50 nm) polythiophene layers. This work was published in Ref. 38.

2.1.1 Materials and Methods

This system consists of vertically-oriented quarter-wavelength gold nanorods (AuNR) placed above a semiconducting sub-50 nm P3HT film on an Ag layer or "conductive ground plane" (Fig.1). To fabricate the desired system, Au was thermally evaporated through a 600-nm-thick, through-hole nanoporous anodic alumina (AAO) mask onto a substrate comprised of P3HT spin-coated from chloroform solution onto an optically-thick thermally-evaporated Ag film on glass. The AAO mask had average pore diameters of 60 nm resulting in AuNRs with comparable diameters (Fig. 2a-c) and the P3HT layer thickness was controlled to within 50 nm by altering the concentration of P3HT in chloroform. The AuNRs were cone rather than cylinder shaped due to shadowing by the pores of the AAO mask during gold evaporation. The mean inter-nanocone distance was determined to be 137 nm consistent with the mean inter-AAO-nanopore distance of 136 nm. From Figure 2d,e it is apparent that the AuNR/P3HT/Ag region was almost black in color indicating that it had stronger

absorption in comparison to the P3HT/Ag area (which exhibited the characteristic deep red color of P3HT).

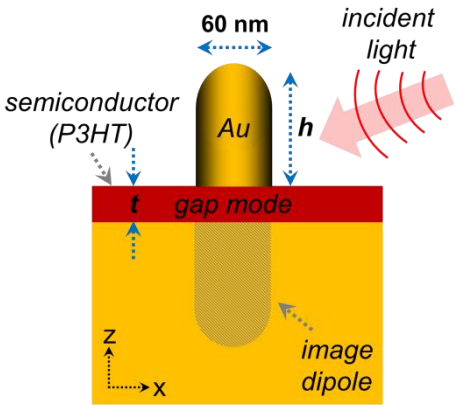

Figure 1. The configuration studied in this work which consists of a vertically-oriented gold nanorod placed on an ultrathin (t ≤ 50 nm) semiconducting polythiophene layers on an optically-thick metal film.

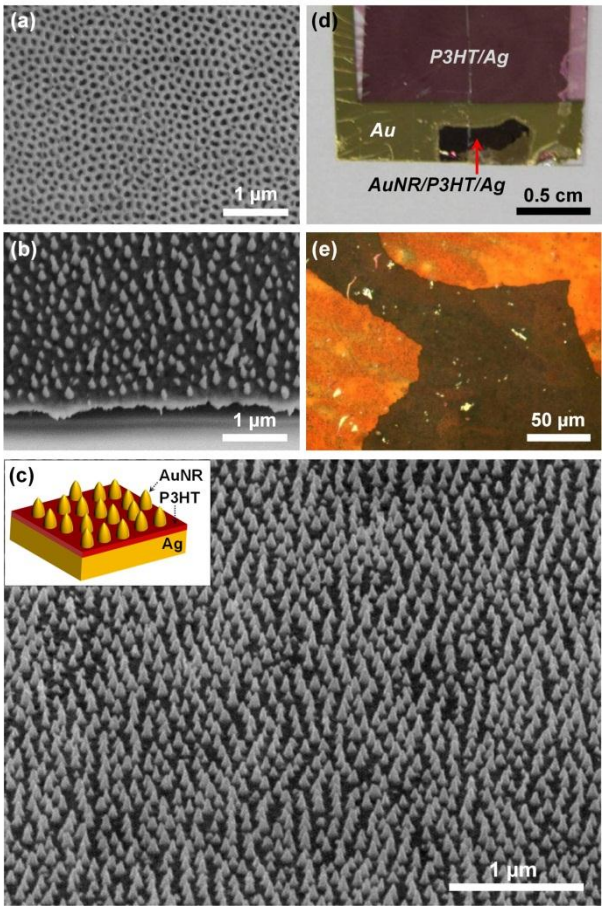

Figure 2. Fabrication of vertically-oriented AuNRs on P3HT/Ag. (a) SEM image of a 600-nm-thick through-hole AAO membrane. (b) SEM image of an array of cone-shaped AuNRs deposited on a ~ 50 nm P3HT thin film on 80 nm of Ag on glass. (c) Main image: larger-area SEM image of an array of AuNRs on a P3HT/Ag film on glass; Inset: Schematic of an AuNR array on P3HT/Ag thin films. (d) Photograph of a sample showing P3HT/Ag and AuNR/P3HT/Ag regions on a glass cover slip (P3HT concentration was 6 g L^{-1}, giving a film thickness of ~ 50 nm). (e) Bright-field reflected-light microscope image acquired within the AuNR/P3HT/Ag region shown in (d).

2.1.2 Enhancement of Semiconductor Absorption

To investigate the optical properties of the P3HT semiconductor layer upon addition of nanorod arrays, extinction spectra (Fig. 3a) from a neat P3HT/Ag film (6 gL^{-1} P3HT in chloroform) and from an AuNR/P3HT/Ag film region (which appeared

black under bright-field microscope imaging; see Figure 2e) were collected by bright-field microscope reflection measurements. The extinction spectra exhibited significant enhancement at the absorption edge of P3HT (660 nm) and a broadened peak (extending more than 250 nm beyond the extinction edge of the P3HT/Ag film spectrum). Furthermore, absorption spectra acquired using an integrating sphere (Fig. 3b), which eliminated the contribution from scattering by the sample, showed similar trends. The consistence of the extinction (i.e., absorption + scattering) and absorption spectra suggested that the broadness of the AuNR/P3HT/Ag film spectra was predominantly due to enhanced light absorption in the sample, relative to the case without the AuNRs. Additionally, the majority of the absorption enhancement occurred at or beyond the absorption band edge of P3HT at 660 nm (Fig. 3b), reaching enhancements greater than a factor of 10 (Fig. 3b, inset).

2.1.3 Theoretical Investigation of Modes Supported by AuNR Arrays on Ultra-thin Polythiophene Layers

To further validate the origin of this significant absorption enhancement, theoretical full-field electromagnetic simulations of the system were carried out for a fixed P3HT thickness of 20 nm, maximum AuNR diameter of 60 nm and for various

AuNR heights, h. Broadband (430 - 800 nm), plane-wave illumination was employed at off-normal incidence (19^{o} - 37^{o}, depending on wavelength) to excite both transverse (x-polarized) and longitudinal (z-polarized) modes of the system; see Figure 4. It was apparent that three main absorption bands in the 430 - 800 nm wavelength range occurred in the AuNRs arising from different mode types (Fig.4a): one at 530 nm was attributed to the characteristic transverse localized surface plasmon resonance of AuNRs [7-13]. This mode was fixed in wavelength, as expected for transverse nanorod resonances, but became relatively more pronounced with increasing nanorod height due to the greater amount of metal present. Another mode occurring between 630 and 700 nm in wavelength was attributed to a gap mode in the P3HT film region under the AuNR [14-16]. A third mode type occurred above 670 nm and was attributed to longitudinal monopole nanorod antenna resonances because the mode wavelength red-shifted with increasing nanorod [7-13]. Both half-wave and higher-order longitudinal antenna resonances were expected to occur for larger nanorod aspect ratios.

The electric-field intensity profiles of the different mode types elucidate how the electric fields are localized around the AuNR and in the P3HT thin film for each mode (top three images of Figure 4). It was apparent that for the gap mode (center image) and longitudinal mode (right image), part of the light was localized in the P3HT region

underneath the AuNR. But for the latter case, the mode wavelength was above the absorption band edge of P3HT and did not contribute significantly to P3HT film absorption enhancement. However, the gap mode, which occurred at a relatively constant wavelength (due to the fixed P3HT film thickness) near the absorption band edge of P3HT, likely gave rise to absorption enhancement in the P3HT film. Figure 3b is a plot of absorption spectra for a 20-nm-thick P3HT region under an AuNR for three different AuNR heights, and for the case without any AuNR. Again, it identifies the significant increase in absorption in the P3HT thin film at 640 nm with addition of AuNR. Additionally, the peak of P3HT absorption in the presence of the AuNR was relatively constant with h, which is consistent with gap-mode absorption enhancement in the P3HT film.

Figure 4c is a plot of integrated absorption in an AuNR and the P3HT region directly underneath the AuNR as a function of AuNR height, h (absorption was integrated over the wavelength range 430 – 800 nm). Unlike the absorption in AuNR, which increases notably and continuously, for h > 40 nm the P3HT film integrated absorption saturated, suggesting that 40-nm-high AuNRs were sufficient for optimum P3HT absorption enhancement. In general, we believe that nanoantennas with lower aspect ratio are most suitable for gap mode enhancement. In addition, slight oscillations in the integrated absorption of the AuNR were observed at h values of 80

nm and 160 nm indicating the contribution to AuNR absorption from height-dependent, z-polarized, longitudinal dipole/multipole resonant modes.

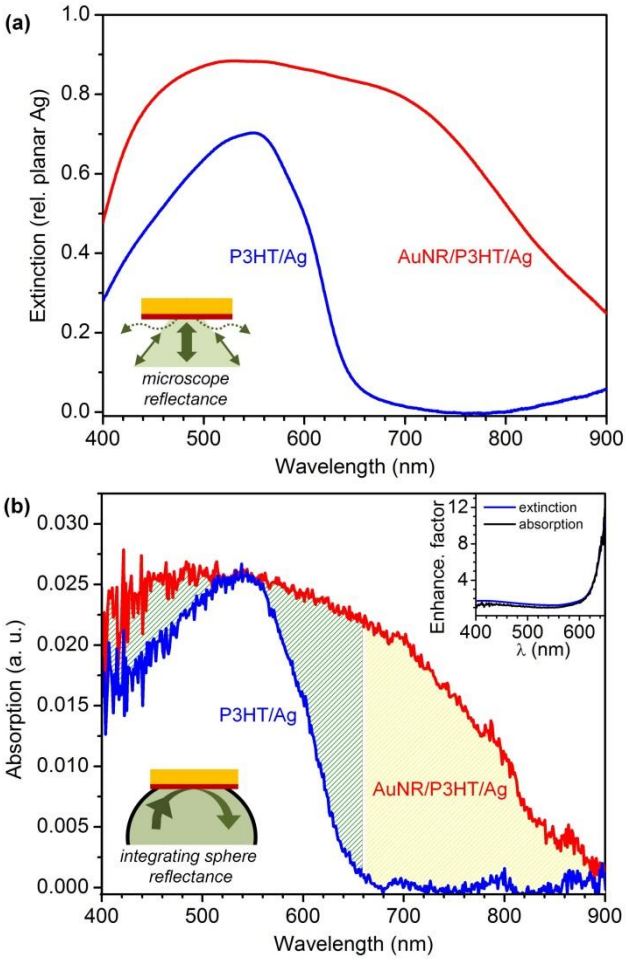

Figure 3. (a) The extinction spectra (acquired using a reflectance microscope coupled to a spectrometer; see inset – dotted arrows represent scattered light not collected) from a P3HT/Ag film region and an AuNR/P3HT/Ag region of the sample shown in Figure 1(d). (b) Absorption spectra acquired using integrating sphere reflectance measurements (see inset) acquired from the same sample used in (a). Bottom left insets in (a) and (b): Schematics of experimental setup. Top right inset in (b): Enhancement in extinction/absorption without/with the integrating sphere.

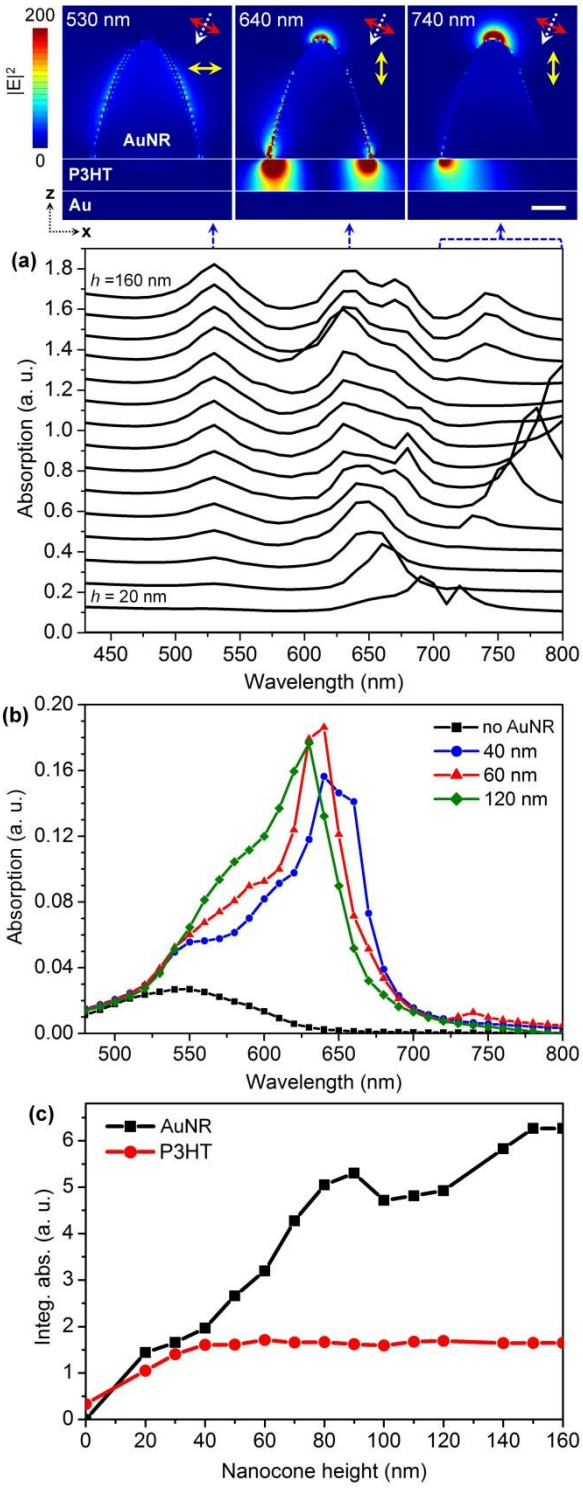

Figure 4. Top images from left to right: Theoretical electric field intensity cross-sections through an AuNR/P3HT/Au monopole nanoantenna system under off-normal (white dashed arrow) plane wave illumination polarized in the direction indicated by the red arrow. AuNR height is 70 nm. The leftmost cross-section displays x-polarized electric field intensity at a free-space wavelength of 530 nm; the center and right-most cross-sections display z-polarized

electric field intensity at free-space wavelengths of 640 nm and 740 nm, respectively. Scale bar is 20 nm. (a) Theoretical absorption spectra for AuNRs with varying height, *h* (bottom curve is for *h* = 20 nm and top curve is for *h* =160 nm with 10 nm increases in *h* in between; AuNR base diameter was 60 nm). (b) Theoretical absorption spectra for the P3HT film region directly under the AuNR, for different *h* values. (c) Theoretical integrated absorption in the AuNR (squares) and P3HT (circles) integrated over the wavelength range 430 nm to 800 nm as a function of *h*. All theoretical data was acquired using 3-dimensional full-field finite-difference-time-domain simulations with plane-wave excitation at an incident angle between 19° to 37° off-normal incidence (incident angle varied within this range with excitation wavelength).

2.2 Effect of Single Nanoparticle Gap Modes on the Optical Properties of Conjugated Polymer Thin Films

In the former section, we theoretically confirmed that gap modes are of crucial importance to absorption enhancement in ultra-thin polymer films. However, experimental validation and identification of how the gap mode wavelength, intensity and degree of light localization can be optimized by changing factors such as: gap thickness; nanoparticle height; or material type is still needed. Here, we seek to investigate gap mode resonances for single nanoparticles characterized by dark-field spectroscopy for an Ag NP/P3HT/Ag film system in combination with scanning electron microscopy (SEM) and atomic force microscopy (AFM) to determine the physical parameters of the system.

2.2.1. Materials and Methods

To fabricate the desired system, in a typical run, a piece of Si substrate/wafer was pre-cleaned by sonication in Sparkleen solution (purchased from Fischer Scientific) and isopropyl alcohol (IPA) for 20 min., respectively. Then a thin layer of Ag was deposited onto the substrate by thermal evaporation. The layer thickness was controlled by measurement with a quartz crystal monitor for the purpose of making it optically thick (transmittance <0.0066 % for 120 nm Ag film at 650 nm wavelength, estimated from the Lambert-Beer Law) and avoiding unnecessary coupling to waveguide modes of the underlying Si upon light illumination. The Ag layer was typically 150 nm thick while the deposition rate was controlled to be under 1 nm/s. Subsequently, the P3HT (purchased from American Dye Source.) in chlorobenzene solution was heated to 60 ℃, stirred for 15 minutes, sonicated for another 20 minutes, filtered (using a 0.2 μm filter) and then spin-coated onto the Ag layer, for which the concentration was varied between 1 g/L and 20g/L. After drying in a desiccator for 20 min., Ag nanoparticles of different sizes (purchased from NanoComposix) with controlled diameter; nanoparticle surface was coated with polyvinyl pyrrolidone (PVP) and the solvent was Milli-Q water) were drop- deposited on the P3HT film on Ag. After

drying for 2 h, the sample was ready for characterization

2.2.2. Thin Film Thickness Measurements

Since we are looking for optical field enhancement in ultra-thin P3HT films, control of the film thickness is of crucial importance. Both cross-sectional SEM and AFM measurements were carried out to establish a reliable method to determine the P3HT film thickness. In the case of SEM, we made a metal/P3HT/metal sandwich structure and different P3HT concentrations were applied for thin film formation: 1 g/l, 2 g/l, 5 g/l, 10 g/l. Once cross-sectional SEM images were obtained, P3HT thickness measurements were made simply by measuring the distance between the two metal planes, as shown in Figure 5. The measured thicknesses are listed in Table 1 (detailed data is shown in the Appendix), and we can see the almost linear relationship between the P3HT layer thickness and the corresponding P3HT concentration used for thin film formation. Aside from that, we also conducted AFM thickness measurements for P3HT films spin coated from different solution concentrations. We first measured the thickness of the thermally evaporated Ag film substrate (in this case we only deposited 60~80 nm thick Ag) and then spin-coated P3HT on top. Measurements of the thickness of the Ag film coated with P3HT were

then carried out. The P3HT film thickness was obtained by subtracting the thickness of the Ag film from the thickness of the P3HT-on-Ag film. All of the AFM thickness measurements were near where a region of the P3HT/Ag film was removed from the Si surface using stainless steel tweezers. Interestingly, the thickness obtained from AFM measurements (Figure 6) was quite different from the thickness obtained from SEM measurements. For the 10 g/l P3HT concentration, the thickness obtained (Table 1) by AFM was only 30.5 nm compared with the thickness of 78.8 nm by SEM. We are still contemplating the reason for this inconsistency but more AFM measurements are needed to verify the reliability of the data. We also carried out thickness measurements for a sample made on SiO_2 rather than Si substrates but the results were not satisfactory because of Ag film degradation and high surface roughness so those results are not reported here.

2.2.3. Single Particle Dark-field Microscopy and Spectroscopy

The single nanoparticle dark-field imaging and spectroscopy measurements were carried out for individual Ag nanospheres using dark-field reflected-light microscopy (Fig. 7), which ultimately required inter-particle distance to be at least 1 μm to avoid inter-particle optical coupling. Several approaches were carried out to deposit

commercially-available Ag NPs on the film. First, we used a spin-coating technique: essentially, the Ag NP solution was spin coated on the P3HT/Ag film (deionized water as solvent) at 6000 rpm for 1 min. But on account of the hydrophobicity of the polymer film, usually all of the particles were cast away with the water and no nanoparticles were left on the P3HT film. We then tried to replace water with a mixture of water/ethanol, water/IPA, water/acetone, but none of them gave satisfactory deposition of NPs on the P3HT. Then drop-deposition directly from the as-purchased Ag NP solution was carried out, but direct deposition lead to severe aggregation of nanoparticles (Fig. 8a). Therefore, a dilution step was necessary and we found that to get the optimized nanoparticle deposition with inter nanoparticle spacing of at least 1 μm, the as-purchased AgNP solution needed to be diluted by 20-30 times. Then 40-60 μl of the diluted AgNP dispersion was drop-deposited on the P3HT film to form a hemi-spherical droplet (after spin-coating of P3HT, the sample needed to be dried under vacuum for 20 mins. to avoid corrosion of the P3HT film by the drop-deposited Ag NP solution). After drying for ~1.5 hrs, the deposited Ag NP region had a relatively good area of quasi-uniformly distributed and discrete Ag NPs suitable for single nanoparticle optical studies.

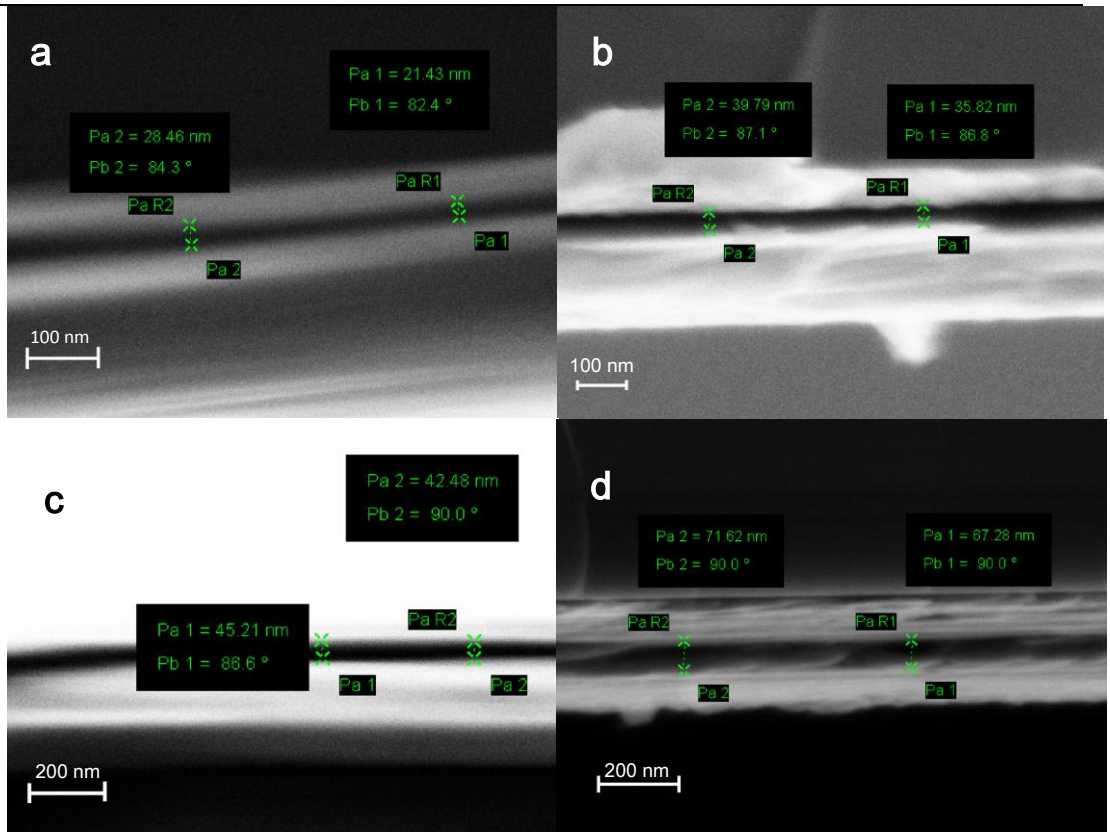

Figure 5: SEM images of the different-concentrated P3HT cross-sections with both sides coated with Ag, the concentrations are (a) 1 g/l, (b) 2 g/l, (c) 5g/l and (d) 10g/l, respectively.

Concentration (g/l)	1	2	5	10	20
P3HT film thickness (SEM results) (nm)	28.64±6.01	39.27±10.69	53.08±11.78	78.76±13.41	
P3HT film thickness (AFM results) (nm)				30.5±8.44	39.5±4.01

Table 1: Different P3HT layer thickness corresponds to various concentrations. SEM Data was obtained by drawing measurement lines from Ag film/P3HT/Ag film sandwich structures on the images. 9, 20, 27, 14 measurements were

taken for concentrations of 1 g/l, 2 g/l, 5 g/l, 10 g/l, respectively. AFM data was post-processed using Gwyddion software and leveled to flatten the pure Si area. Here 15 and 25 measurements were taken for concentrations of 10 g/l and 20 g/l, respectively

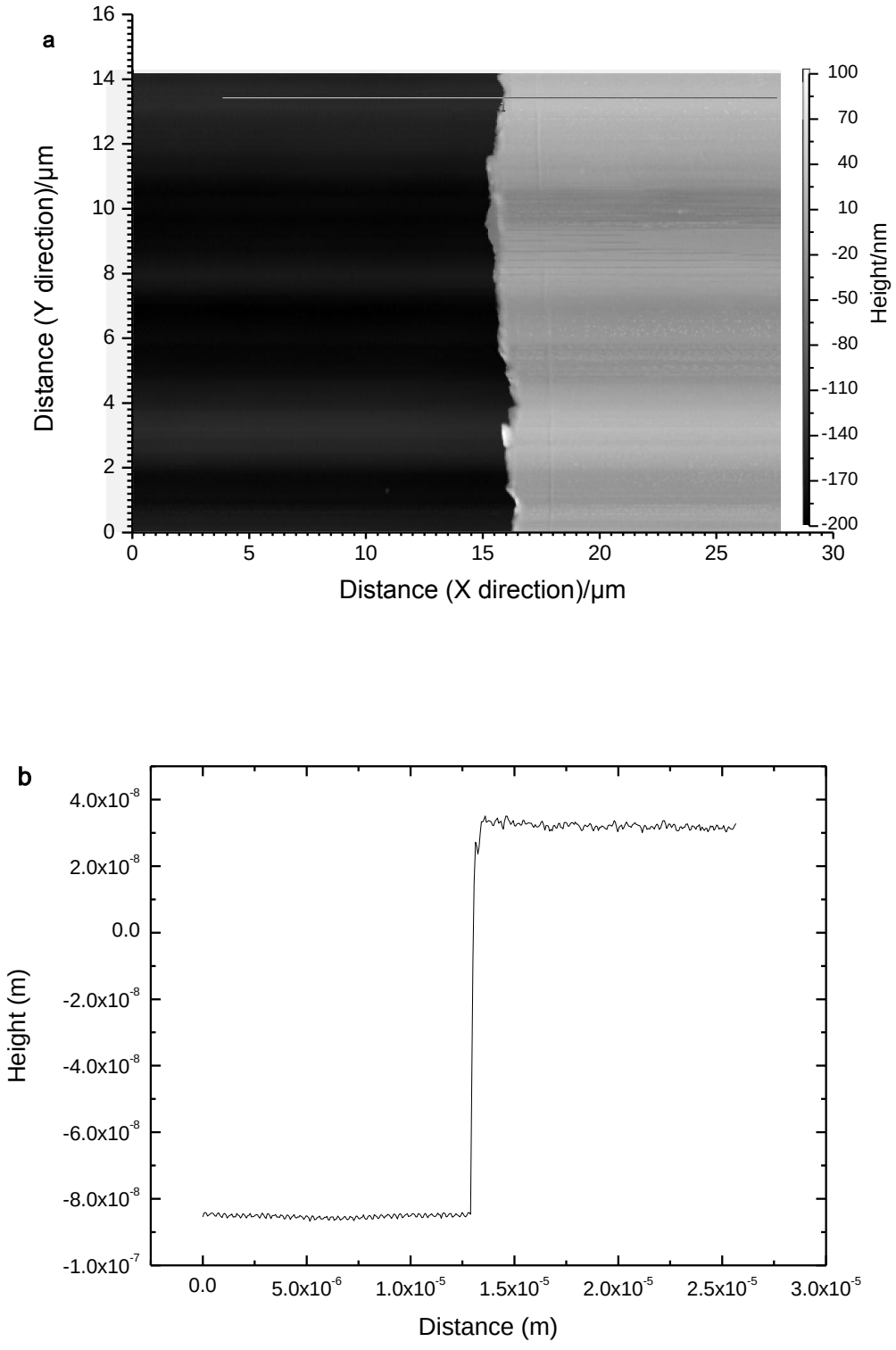

Figure 6. A typical AFM measurement for the sample, as shown is the measurement for the thickness of 20 g/l P3HT

on 60 nm thick Ag (as shown on the thermal evaporator) on Si substrate. (a) The composition image of the sample, the darker area is where we draw the scratch, so it's pure Si, while the brighter part is where Ag and P3HT were deposited. (b) The graph of the height offset.

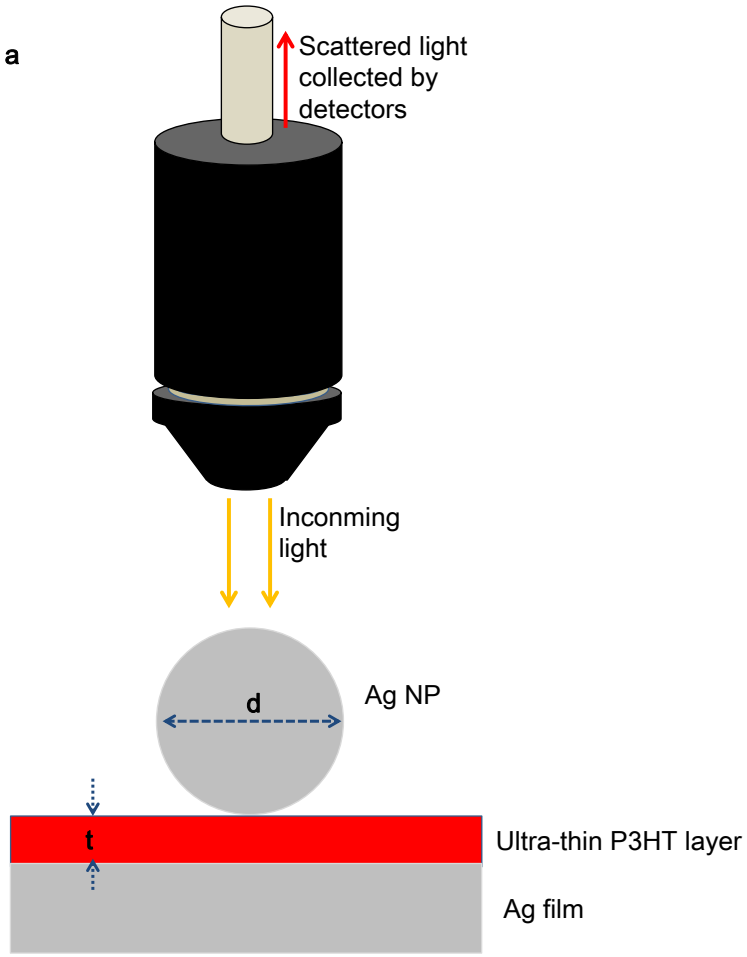

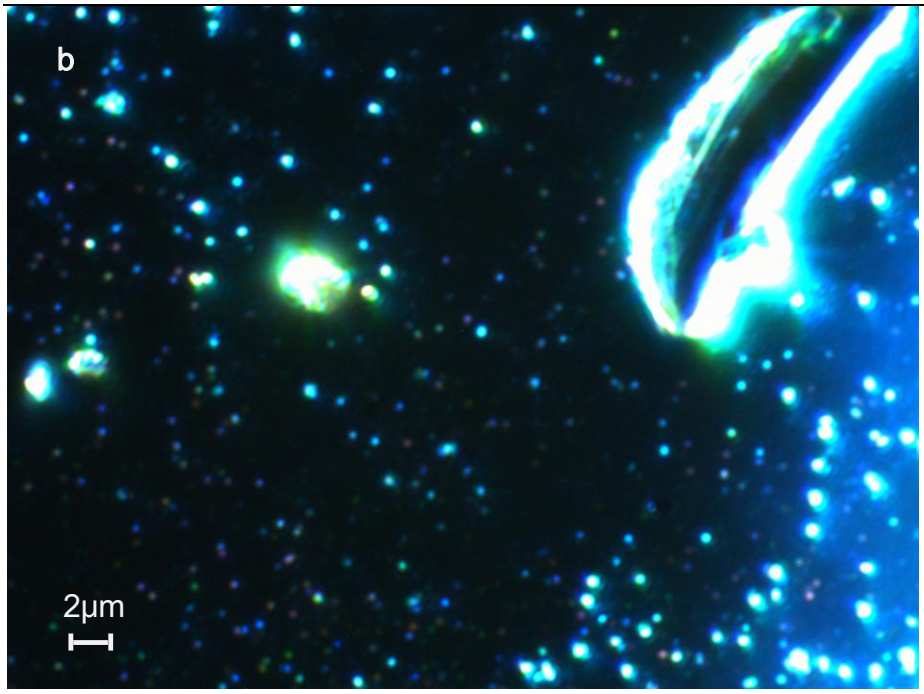

Figure 7: (a) Schematic of dark field microscopy of single nanoparticles. Incident light (from a Xenon lamp) was incident normal to the sample and scattering patterns were collected by the detectors on top. An imaging spectrometer was properly aligned to the microscope to obtain optimized resolution. Both the diameter, d, of the Ag NP and the thickness, t, of the P3HT layer can be altered. (b) 40X dark-field scattered light microscopic image of Ag NP with 100 nm diameter on top of 5g/L P3HT on Ag film, which shows distinct nanoparticles

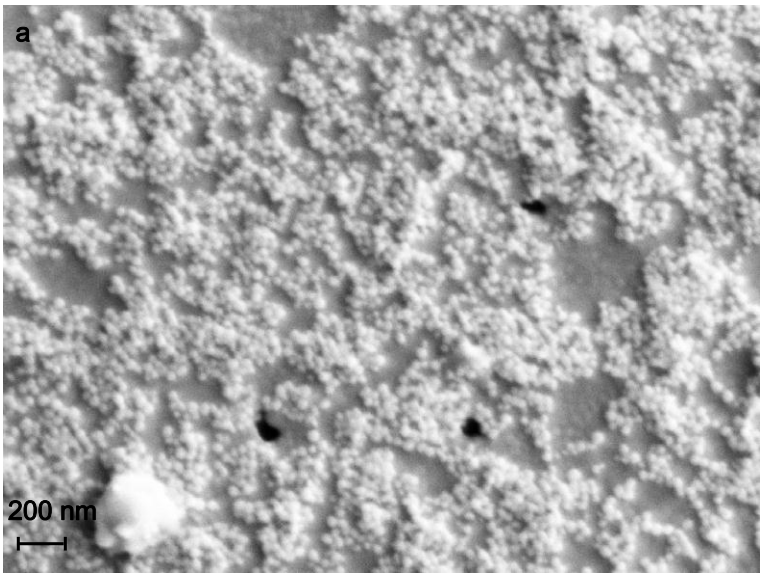

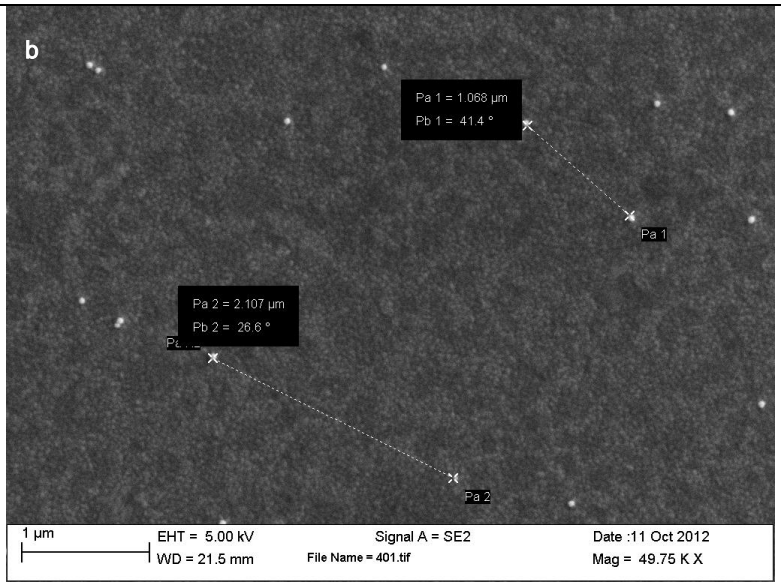

Figure 8. SEM images of Ag nanoparticles on a P3HT film on Ag. (a): Direct drop-casting of the stock solution on the P3HT film, which shows massive conjugation of the particles. (b): Drop-casting of a 30X diluted 40 nm Ag NP solution - the inter-particle distance is sufficient to conduct single particle imaging and spectroscopy measurement.

3. Thesis Objectives and Future Work

Aside from finishing the single particle gap mode investigation described in the previous section, there are several other goals I propose to achieve before graduation.

3.1 Device Construction and Photocurrent Measurements

Based on the absorption enhancement in underlying P3HT material by addition of nanoantenna arrays, our ultimate goal is to build a device out of the current structure

to carry out photocurrent measurements. First we will fabricate a conventional bulk heterojunction device consisting of a conjugated polymer/fullerene ultra-thin active layer (~20 nm); see Scheme 1 [43]. Alternatively, we may change the p-type buffer layer (hole transport layer) and n-type buffer layer (electron transport layer) to fabricate an inverted device, which is expected to show improved device stability in ambient conditions [42].

The first proposed structure (Scheme 1) consists of Ag/Al as cathode electrode with relatively low work function of 4.2 eV, this provides an ohmic contact at the cathode-fullerene interface since the lowest unoccupied molecular orbital (LUMO) level ofPhenyl-C61-butyric acid methyl ester (PCBM) is 4.3 eV [43]. On top of that will be an ultra-thin active layer, which may consist of a P3HT/PCBM blend. The thickness of the active layer will be controlled to be less than 50 nm. A p-type interface layer of poly(3,4-ethylenedioxythiophene): poly(styrenesulfonate) (PEDOT:PSS) (thickness of ~10 nm; work function of ~4.7 eV) will be applied on top of the active layer to form an ohmic contact with the photoactive layer for effective hole collection (highest occupied molecular orbital (HOMO) level of P3HT is ~5.0 eV), which will act as a hole transport layer. Then Au nanoantenna arrays will be were thermally evaporated on top of the PEDOT:PSS layer via a through-hole AAO membrane. The reason we will use Au instead of Ag nanoantennas is that the cathode material, either Al or Ag has a work

function of about 4.2 eV, if Ag nanoantennas were applied, there would not be a sufficient potential difference between the nanoantenna and the cathode for effective charge collection to occur. In other words, electrons will have a greater chance to diffuse to the anode side, causing electron-hole recombination. Finally, on the anode side, a layer of a transparent conducting oxide (TCO) material, such as indium-tin oxide (ITO) or ZnO (applied by sputter coating or solution-based methods), which has a work function of ~4.7 eV. We anticipate that this device structure will give a repeatable photocurrent response, but certain drawbacks of this structure may be as follows:

1. The acidic nature of PEDOT:PSS may causes issues regarding the long-term stability of the device and photocurrent measurements. To get around this problem, various transition metal oxides may be introduced [43], such as V_2O_5, M_OO_3, WO_3 and NiO, as a replacement to PEDOT:PSS. Besides, solution-processed transition metal oxides have recently also become popular for use in organic photovoltaics [43,44]. The only problem of using transition metal oxides is the HOMO offset at the organic molecule/metal oxide interface, which is of crucial importance to electron/hole transfer. A global picture of oxide/organic energy alignment is not yet available, but researchers have pointed out that Fermi-level-pinning transition is a universal trend [45].

Essentially, this means energy alignment can be established regardless of oxide conduction/valence band position, but directly related to the Fermi level of oxide. Traditionally, for a hole to transfer from an organic molecule to an oxide, the hole must move from the organic molecule's HOMO level into the oxide's conduction band, yet due to Fermi-level-pinning, organic molecule's HOMO level can become pinned to the Fermi level of the oxide even if the HOMO level is far away from the oxide's conduction or valence bands. Theoretically, by tuning the doping conditions of oxides, the Fermi level could be altered and energy alignment may be achieved.

2. For the aforementioned structure, there will be the direct contact of Au nanoantenna arrays with ITO or ZnO which may enable the nanoantennas to act as electrical contacts with photocurrent following through the metal nanostructure. Since both ITO and ZnO are typically n-doped semiconductors, this might lead to a Schottky Barrier at the nanoantenna TCO interface [46,47]. Unlike P-N junctions, electron-hole recombination is not involved in Schottky barriers, which essentially eliminate the depletion zone, and thus result in a smaller junction voltage (0.15-0.45 V) compared to P-N junctions (0.6-1.7 V), as well as higher switching speed (~100 ps in comparison with over 100 ns for P-N junction) [47]. However, the detailed working mechanism of nanoantenna

contacts still needs further clarification.

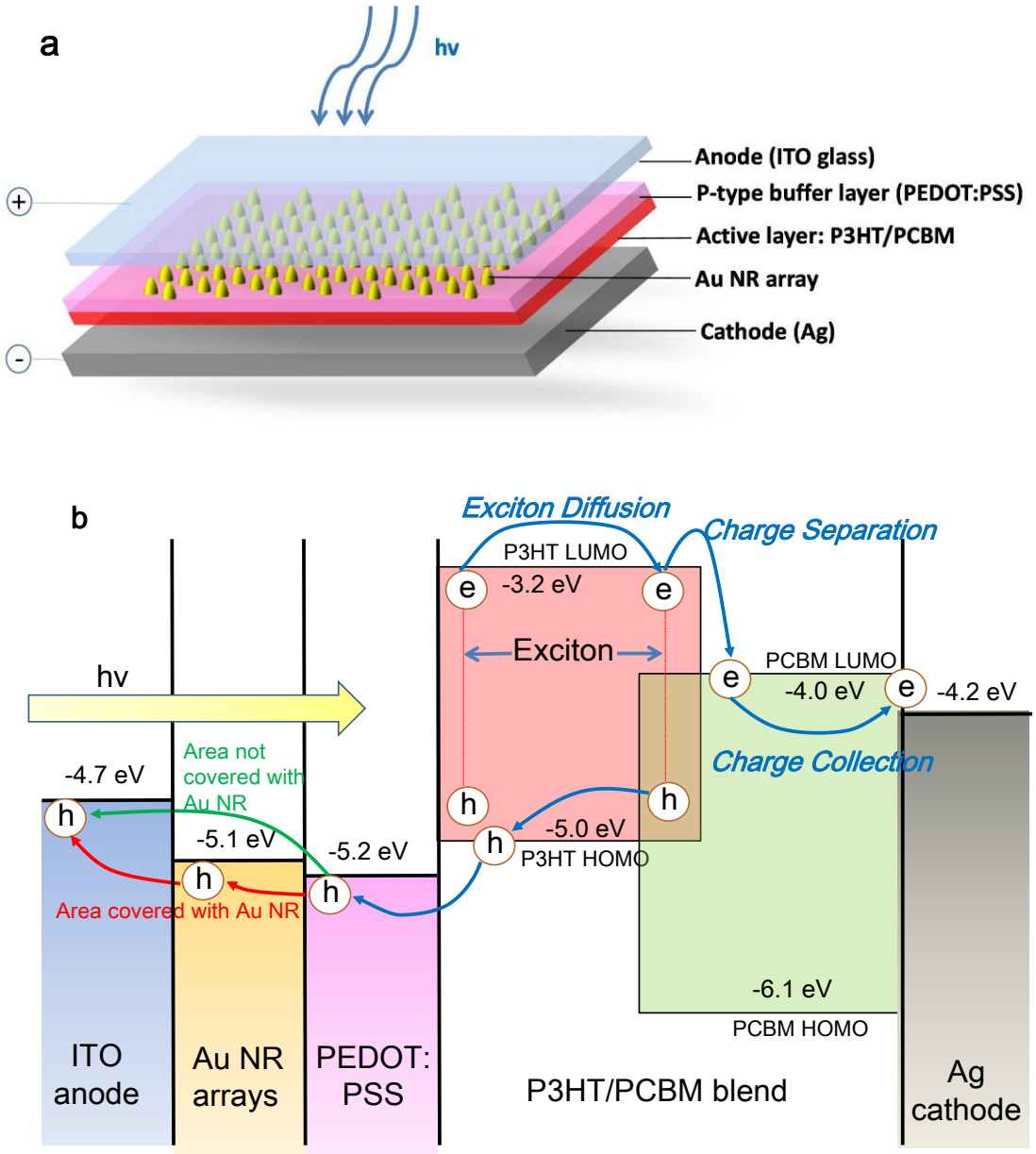

Scheme 1. (a) The first proposed structure of an organic photovoltaic device with an ultra-thin active layer and incorporating nanoantennas placed on top built out of Au nanorod arrays. (b) The operating mechanism of the above photovoltaic device.

The second structure (Scheme 2) is similar to the first one, the only difference lies in the replacement of the hole transport layer with an electron transport layer inserted between the active layer and cathode. A typical material for n-type electron transport layers is sol-gel-based TiOx [23,45] Low-temperature (150 ℃) hydrolysis sol-gel processing of amorphous TiOx has been shown to function as a hole-blocking layer and an optical spacer, which enhances absorption inside a thin device by modulating the optical field [23]. Other groups have shown the use of TiOx spacers lead to 40% enhancement in photocurrent and external quantum efficiency (EQE) for a P3HT:PCBM system [23]. Another advantage of TiOx is that its LUMO level (~4.2 eV) aligns perfectly with Al cathodes.

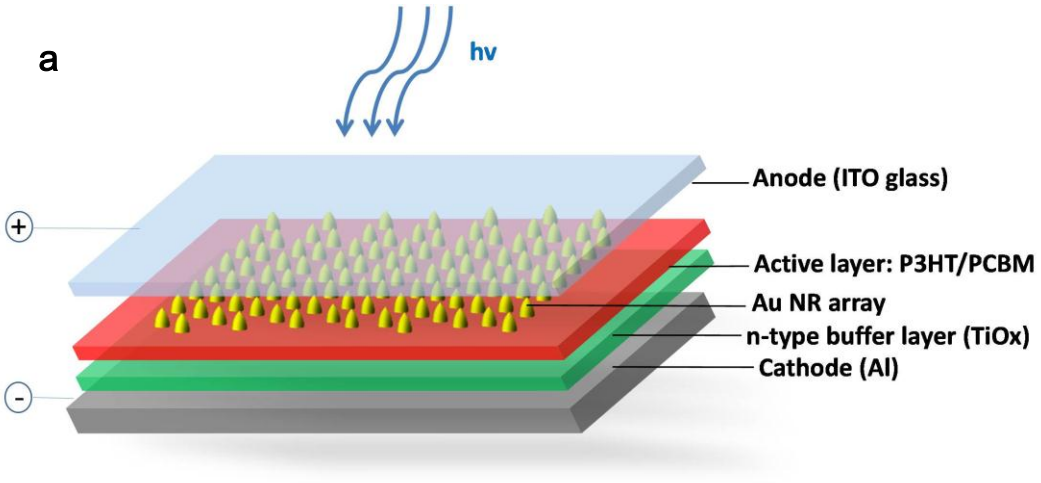

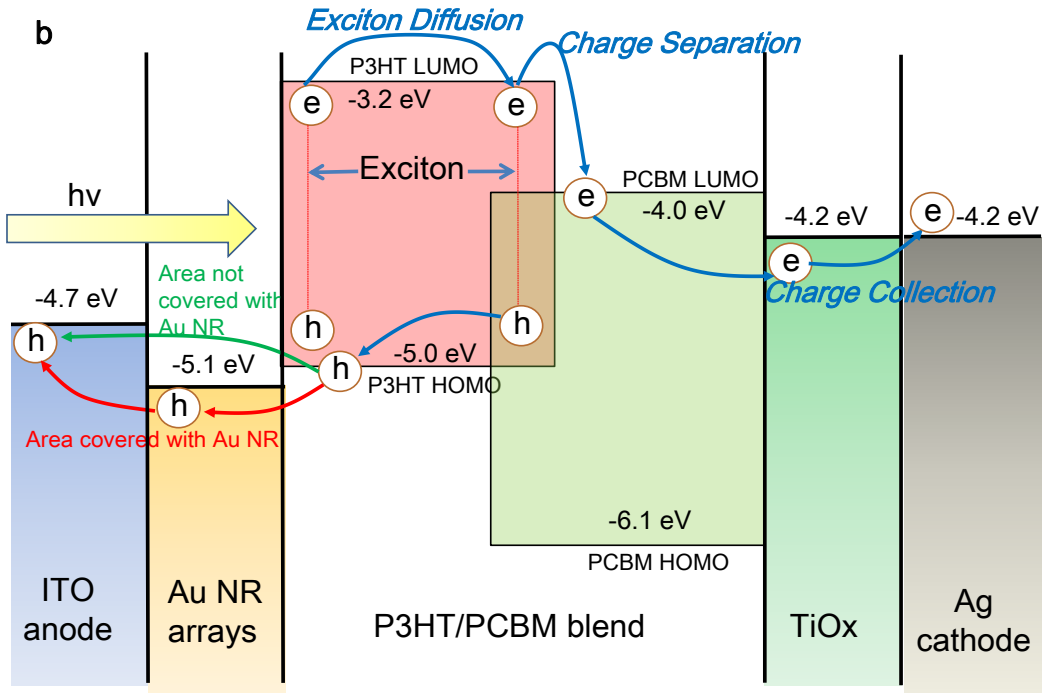

Scheme 2. (a) The second proposed structure of an organic photovoltaic device with an ultra-thin active layers and incorporating nanoantennas placed on top built out of Au nanorod arrays. (b) The operating mechanism of the above photovoltaic device.

Ultimately, we can combine the two proposed structures shown in Scheme 1 and 2 (meaning using both a hole transport and an electron transport layer) to achieve best device performance, but this will add fabrication difficulty as well as bring in more variables. Initially, the two proposed structures will be fabricated separately and optimized by controlling parameters such as film thickness and size, aspect ratio and packing density of nanoantenna arrays. We will also conduct some full-field electromagnetic simulations to support our experimental work.

The third proposed structure to measure photocurrent arising from application of

nanoantennas to ultra-thin conjugated polymer layers, uses graphene instead of other transparent conducting oxides; see Scheme 3. Here we put a graphene anode underneath the Au NRs because of the limitation of the fabrication technique (large area graphene needs to be deposited by chemical vapor deposition (CVD) on Si or Cu substrates then transferred onto the as-prepared sample, which requires smoothness of the underlying substrate) which essentially means the Au NRs are purely for field enhancement here. Researchers have shown 55% power conversion efficiency (PCE) enhancement of graphene-based organic photovoltaic devices over ITO-based devices due to the outstanding conductivity and optical transparency properties of graphene [48]. Although the work function of grapheme is 4.2 eV while the HOMO level of P3HT is 5.2 eV which implies a large hole-injection barrier, the Fermi energy of graphene can be easily tuned by doping. However, the major drawback of graphene films is their poor hydrophilicity, which could lead to a negative effect on the construction of solution-processed devices [49]. This could be improved by possible surface modification by chemical functionalization method [50]. The other unknown aspect the proposed structure is the effect of graphene-metal nanoantennas on photocurrent measurements. Research has shown that decoration of graphene with metal nanoparticles will result in strong electronic interactions (charge transfer) between two [51,52,53]

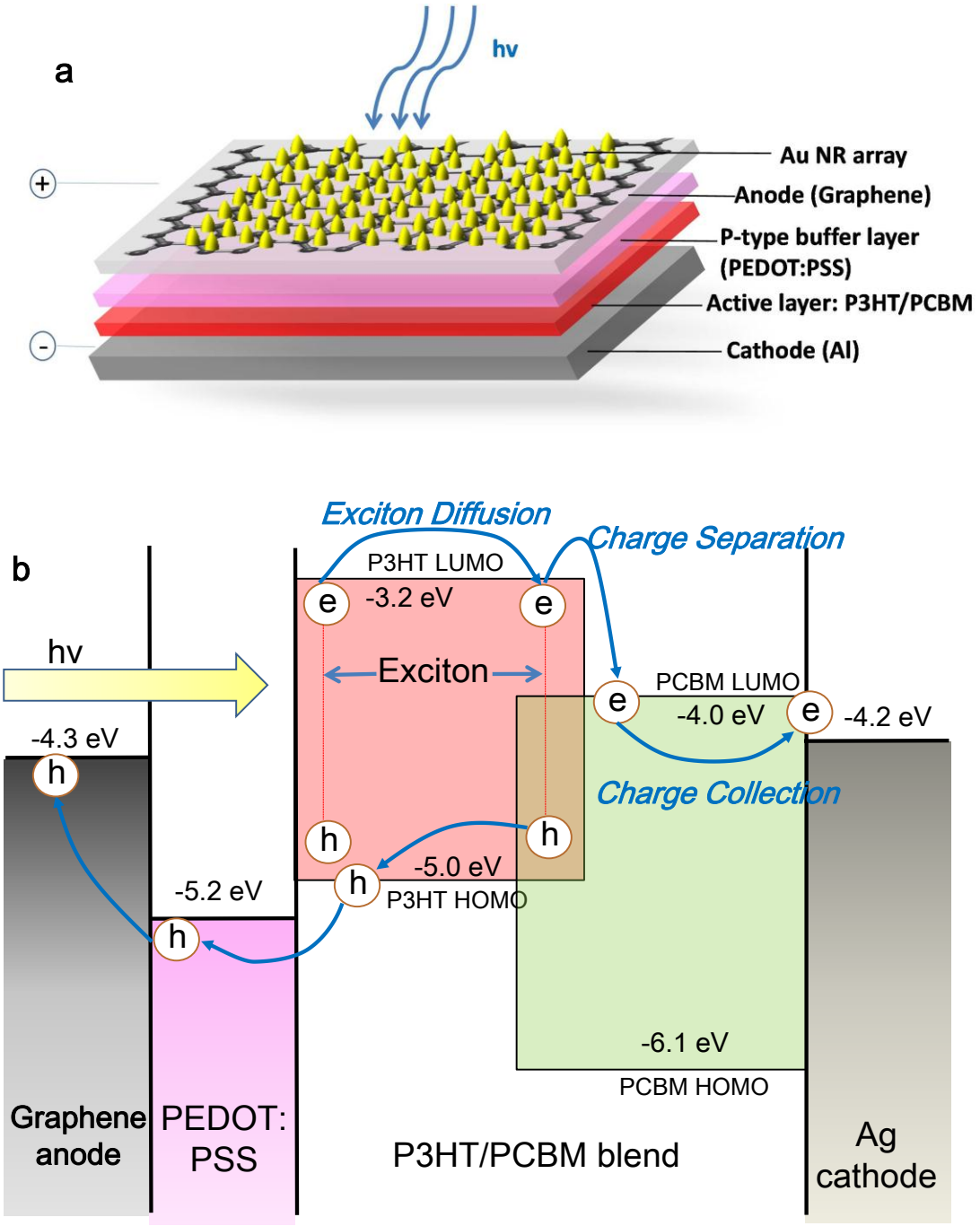

Scheme 2. (a)The third proposed structure of an organic photovoltaic device with an ultra-thin active layer and incorporating nanoantennas placed on top built out of Au nanorod arrays. (b) The operating mechanism of the above photovoltaic device.

3.2 Internal Photoemission Study

In the former study, we will essentially take advantage of the strong near-field enhancement of metal nanostructures to improve the performance of ultra-thin-active-layer optoelectronic devices. While another important property of optical nanoantennas which has recently received significant attention is the propensity for generating “hot” electron-hole pairs (EHP) at a metal/semiconductor interface by surface plasmon decay [47]. This process is usually considered deleterious to nanoantenna performance because it’s an external contribution to plasmon damping, but our preliminary work has shown that a significant portion of incident light is absorbed by Au nanorods themselves. In theory, if all of the light not redirected by the antenna into the semiconductor is used to form electron-hole pairs in the nanoantenna, this process could lead to injection of plasmon excited “hot” electrons from metal nanostructures into the semiconductor and may be collected as photocurrent [46] The injected electrons are not expected to be limited by the band gap of the semiconductor, the only barrier would be the Schottky barrier which forms at metal/semiconductor interface, which means the exploitation of photon energy below the band gap and could undoubtedly enhance the efficiency of our thin film based devices [47]. Yet this area is relatively new and we still need to confirm the

presence of hot electron effects in the proposed devices.

3.3 Light-Emitting Applications of Monopole Nanoantennas

Preliminary work done by Prof. O'Carroll has shown that Au-P3HT-Au split dipole nanoantennas have extraordinary performance in enhancing the radiative emission rate as well as improving luminescence quantum efficiency of conjugated polymers [39]. This suggests that the nanoantenna-thin film structures proposed here could be promising configurations for demonstration of light emitting diodes with ultra-thin active layers by simply replacing P3HT with more emissive material such as Poly[(9,9-di-n-octylfluorenyl-2,7-diyl)-alt-(benzo[2,1,3]thiadiazol-4,8-diyl) (F8BT) or poly(9,9-dioctyylfluorenyl-2,7-diyl) (PFO) (Scheme 4). The main issue with this application is to design the nanoantenna in a way that avoids light trapping and improves light out-coupling from the polymer layers which is exactly the opposite of what we want to achieve for photovoltaic applications.

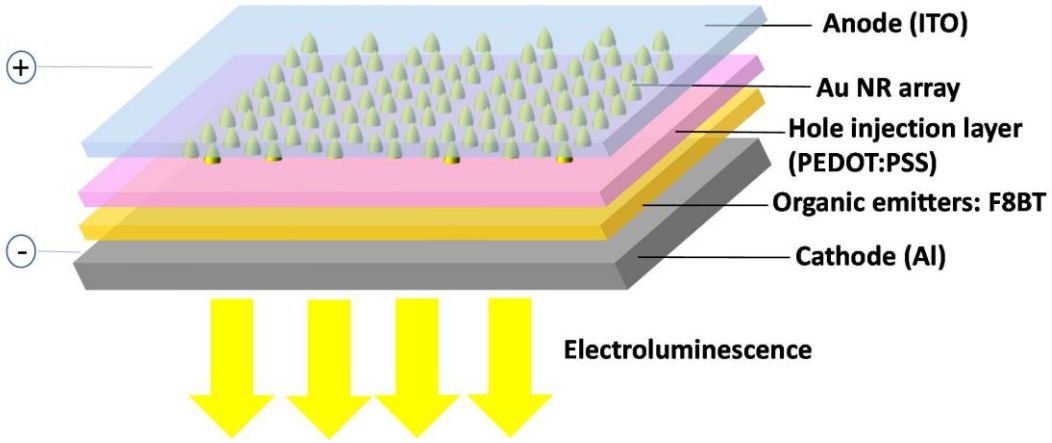

Scheme 4. The structure of an organic light emitting diode device with an ultra-thin active layers and incorporating nanoantennas placed on top built out of Au nanorod arrays.

4. Conclusion

In conclusion, this thesis proposal has studied the absorption changes and plasmonic modes arising from the placement of vertically-oriented, cone-shaped gold nanorod arrays on sub-50-nm thick P3HT films on metallic substrates using experimental and theoretical methods. Both extinction and absorption characterization showed notable enhancement and broadening of the sample extinction and absorption spectra relative to underlying P3HT films on Ag substrate. Different modes of the system affected sample absorption to different degrees. Especially, the gap modes between the nanorod and the ground plane resulted in intense localized fields in the P3HT layers directly underneath the nanorod and gap

mode wavelengths were within the absorption band range of P3HT. Low aspect ratio nanorods were found to exhibit the lowest metal absorption losses in this particular system. Also our systems are applicable to ultra-thin optoelectronic device where control of light interactions and mode coupling in the active layer are critical to device performance. The proposed work includes building the thin-film device such as organic photovoltaics, organic light emitting diodes as well as internal photoemission study out of our current structure. Detailed working mechanism and device configurations were shown and discussed which essentially all take advantage of the strong near-field enhancement around nanoantennas to improve device efficiency. This work has identified conditions for optimal light-management in ultra-thin semiconductor films embedded in a monopole antenna system and paved the road for future thin-film based high efficiency optoelectronic devices.

5. References

1. E. Yablonovitch and G. D. Cody, "Intensity enhancement in textured optical sheets for solar-cells," IEEE Trans. Electron. Dev. 29(2), 300–305 (1982).

2. H. Kiess and W. Rehwald, "On the ultimate efficiency of solar-cells," Sol. Energy Mater. Sol. Cells **38**(1–4), 45–55 (1995).

3. A. V. Shah, R. Platz, and H. Keppner, "Thin-film silicon solar-cells—a review and selected trends," Sol. Energy Mater. Sol. Cells **38**(1–4), 501–520 (1995).

4. C. Heine and R. H. Morf, "Submicrometer gratings for solar-energy applications," Appl. Opt. **34**(14), 2476–2482 (1995).

5. J. Zhao and M. A. Green, "Optimized antireflection coatings for high-efficiency silicon solar-cells," IEEE Trans. Electron. Dev. **38**(8), 1925–1934 (1991).

6. J. H. Zhao, A. H. Wang, M. A. Green, and F. Ferrazza, "19.8% efficient "honeycomb" textured multicrystalline and 24.4% monocrystalline silicon solar cells," Appl. Phys. Lett. **73**(14), 1991–1993 (1998).

7. E. Yablonovitch, "Statistical ray optics," J. Opt. Soc. Am. **72**(7), 899–907 (1982).

8. K. Tvingstedt, N.-K. Persson, O. Inganas, A. Rahachou, and I. V. Zozoulenko, "Surface plasmon increase absorption in polymer photovoltaic cells," Appl. Phys. Lett. **91**(11), 113514 (2007).

9. C. Hägglund, M. Zach, G. Petersson, and B. Kasemo, "Electromagnetic coupling of light into a silicon

solar cell by nanodisk plasmons," Appl. Phys. Lett. **92**(5), 053110 (2008).
10. P. Matheu, S. H. Lim, D. Derkacs, C. McPheeters, and E. T. Yu, "Metal and dielectric nanoparticle scattering for improved optical absorption in photovoltaic devices," Appl. Phys. Lett. **93**(11), 113108 (2008).
11. K. Nakayama, K. Tanabe, and H. A. Atwater, "Plasmonic nanoparticle enhanced light absorption in GaAs solar cells," Appl. Phys. Lett. **93**(12), 121904 (2008).
12. S. S. Kim, S. I. Na, J. Jo, D. Y. Kim, and Y. C. Nah, "Plasmon enhanced performance of organic solar cells using electrodeposited Ag nanoparticles," Appl. Phys. Lett. **93**(7), 073307 (2008).
13. A. J. Morfa, K. L. Rowlen, T. H. Reilly III, M. J. Romero, and J. Van De Lagemaat, "Plasmon-enhanced solar energy conversion in organic bulk heterojunction photovoltaics," Appl. Phys. Lett. **92**(1), 013504 (2008).
14. N. C. Lindquist, W. A. Luhman, S.-H. Oh, and R. J. Holmes, "Plasmonic nanocavity arrays for enhanced efficiency in organic photovoltaic cells," Appl. Phys. Lett. **93**(12), 123308 (2008).
15. C. Hägglund, M. Zach, and B. Kasemo, "Enhanced charge carrier generation in dye sensitized solar cells by nanoparticle plasmons," Appl. Phys. Lett. **92**(1), 013113 (2008).
16. F.-J. Haug, T. Söderström, O. Cubero, V. Terrazzoni-Daudrix, and C. Ballif, "Plasmonic absorption in textured silver back reflectors of thin film solar cells," J. Appl. Phys. **104**(6), 064509 (2008).
17. R. A. Pala, J. White, E. Barnard, J. Liu, and M. L. Brongersma, "Design of plasmonic thin-film solar cells with broadband absorption enhancements," Adv. Mater. (Deerfield Beach Fla.) **21**(34), 3504–3509 (2009).
18. H. A. Atwater and A. Polman, "Plasmonics for improved photovoltaic devices," Nat. Mater. **9**(3), 205–213 (2010).
19. Brus, L. Noble metal nanocrystals: Plasmon electron transfer photochemistry and single-molecule Raman spectroscopy. Acc. Chem. Res. 41, 1742–1749 (2008).
20. Nie, S. & Emory, S. R. Probing single molecules and single nanoparticles by surface-enhanced Raman scattering. Science 275, 1102–1106 (1997).
21. Jiang, J., Bosnick, K., Maillard, M. & Brus, L. Single molecule Raman spectroscopy at the junctions of large Ag nanocrystals. J. Phys. Chem. B 107, 9964–9972 (2003)
22. Larsson, E. M., Langhammer, C., Zorić , I. & Kasemo, B. Nanoplasmonic probes of catalytic reactions. Science 326, 1091–1094 (2009).
23. Chou S. Y., Ding W., "Ultrathin, high-efficiency, broad-band, omni-acceptance, organic solar cells enhanced by plasmonic cavity with subwavelength hole array", Optics Express, 21, S1, A60(2012)
24. Kim S. S., Jo Na, J., Kim D. Y., and Nah Y. C., "Plasmon enhanced performance of organic solar cells
using electro deposited Ag nanoparticles," Appl. Phys. Lett. 93(7), 073307 (2008).
25. Lindquist N. C., Luhman W. A., OhS.-H., and Holmes R. J., "Plasmonic nanocavity arrays for enhanced efficiency in organic photovoltaic cells," Appl. Phys. Lett. 93(12), 123308 (2008).
26. H. R. Stuart, and D. G. Hall, "Island size effects in nanoparticle-enhanced photodetectors," Appl. Phys. Lett. 73(26), 3815–3817 (1998).
27. S. Pillai, K. R. Catchpole, T. Trupke, and M. A. Green, "Surface plasmon enhanced silicon solar cells," J. Appl.Phys. 101(9), 093105 (2007).
28. K. R. Catchpole, and A. Polman, "Design principles for particle plasmon enhanced solar cells," Appl. Phys. Lett. 93(19), 191113 (2008).
29. F. J. Beck, A. Polman, and K. R. Catchpole, "Tunable light trapping for solar cells using localized surface plasmons," J. Appl. Phys. 105(11), 114310 (2009).
30. D. Derkacs, S. H. Lim, P. Matheu, W. Mar, and E. T. Yu, "Improved performance of amorphous silicon solar cells via scattering from surface plasmon polaritons in nearby metallic nanoparticles," Appl. Phys. Lett. 89(9), 093103 (2006).
31. P. Matheu, S. H. Lim, D. Derkacs, C. McPheeters, and E. T. Yu, "Metal and dielectric nanoparticle scattering for improved optical absorption in photovoltaic devices," Appl. Phys. Lett. 93(11), 113108 (2008).
32. K. Nakayama, K. Tanabe, and H. A. Atwater, "Plasmonic nanoparticle enhanced light absorption in GaAs solar cells," Appl. Phys. Lett. 93(12), 121904 (2008).
33. I. M. Pryce, D. D. Koleske, A. J. Fischer, and H. A. Atwater, "Plasmonic nanoparticle enhanced photocurrent in GaN/InGaN/GaN quantum well solar cells," Appl. Phys. Lett. 96(15), 153501 (2010).
34.N. Bonod, G. Tayeb, D. Maystre, S. Enoch, E. Popov, Total absorption of light by lamellar metallic gratings, Opt. Express 2008, 16, 15431–15438.

35. N. Yamamoto, S. Ohtani, F. J. Garcia de Abajo, Gap and Mie plasmons in individual silver nanospheres near a silver surface, Nano Lett. 2011, 11, 91–95.
36. K. Kneipp, M. S. Feld et al, Single molecule detection using Surface-Enhanced Raman Scattering, Phys. Rev. Lett. 1997, 78, 1667–1670.
37. Rodrı´guez-Lorenzo, L.;A´ lvarez-Puebla, R. A.; Pastoriza-Santos, I.; Mazzucco, S.; Ste´phan, O.; Kociak, M.; Liz-Marza´n, L. M.; Garcı´a de Abajo, F. J. J. Am. Chem. Soc. 2009, 131, 4616–4618.
38. B. Yu, S. Goodman, A. Abdelaziz, D. M. O' Carroll, Light-management in ultra-thin polythiophene films using plasmonic monopole antennas, Appl. Phys. Lett. 101, 151106(2012).
39. D. M. O' Carroll,et al., Conjugated Polymer-Based Photonic Nanostructures, submitted.
40. A. A. Ercha, D. J. Ripin, S. Fan, P. Rakich, J. D. Joannopoulos, E. P. Ippen, G. S. Petrich and L. A. Kolodziejski, "Enhanced coupling to vertical radiation using a two-dimensional photonic crystal in a semiconductor light-emitting diode", Appl. Phys. Lett., 78, 5, 563(2001)
41. D. Lei, S. Maier et al., Revealing plasmonic gap modes in particle-on-film systems using dark-field spectroscopy, ACS Nano, 6, 2, 1380 (2012).
42. Z. He, C. Zhong, S. Su, M. Xu, H. Wu, Y. Cao, Enhanced power-conversion efficiency in polymer solar cells using an inverted device structure, Nat. Photonics, 6, 591–595(2012).
43.G. Li,R. Zhu, Y. Yang, Polymer solar cells, Nat. Photonics, 6, 153–161(2012).
44. J. J. Benson-Smith, L.Goris, K. Vandewal,K.Haenen, J.V.Manca, D.Vanderzande, D. D. C. Bradley, J. Nelson, Formation of a Ground-State Charge-Transfer Complex in Polyfluorene/[6,6]-Phenyl-C61 Butyric Acid Methyl Ester (PCBM) Blend Films and Its Role in the Function of Polymer/PCBM Solar Cells, Adv. Funct. Mater. 2007, 17,451.
45. M. Greiner, M. Helander, J. Qiu, Z. Lu, Universal energy-level alignment of molecules on metal oxides, Nat. Materials, 11, 76–81(2012).
46. M. Knight, P. Nordlander, N. Halas, Photodetection with active optical antennas, Science 332, 702(2011).
47. C. Scales, P. Berini, Thin-film Schottky barrier photodetector models, IEEE J. Quantum Electron. 46, 633 (2010)
48. F. Bonaccorso, Z. Sun, T. Hasan and A. C. Ferrari, Graphene photonics and optoelectronics. Nature Photonics, 4 , 611 – 622 (2010).
49. Z. Liu, Q. Liu, Y. Huang, Y. Ma, S. Yin, X. Zhang, W. Sun, Y. Chen, Organic Photovoltaic Devices Based on a Novel Acceptor Material: Graphene, Adv. Mater. 2008, 20, 3924–3930.
50. Y. Wang, X. Chen, Y. Zhong, K. P. Loh, Large area, continuous, few-layered graphene as anodes in organic photovoltaic devices, Appl. Phys. Lett. **95**, 063302 (2009)
51. C. Guo, H. Yang, Z. Sheng, Z. Lu, Q. Song, C. Li, Layered Graphene/Quantum Dots for Photovoltaic Devices, Angew. Chem. Int. Ed. 2010, 49, 3014–3017.
52. K.S. Subrahmanyam, A. K. Manna, S. K. Pati, C.N.R. Rao, A study of graphene decorated with metal nanoparticles, Chemical Physics Letters 497 (2010), 70–75
53. C. Xu, X. Wang and J. Zhu, Graphene-Metal Particle Nanocomposites, J. Phys. Chem. C 2008, 112, 19841–19845.

6. Appendix

Concentration	1g/L	2g/L	5g/L	10g/L
	21.43	26.35	49.9	86.7
	28.46	37.92	57.03	75.95
	33.75	30.43	45.68	63.39
	24.12	22.31	39.97	71.62
	22.39	56.31	72.88	67.28
	21.64	66.05	57.52	87.16
	15.29	40.44	78.71	93.53
	20.26	37.56	65.06	82.02
	35.43	39.79	77.25	86.63
		35.82	43.98	76.54

		47.6	71.46	108.6
		44.89	39.51	80
		28.36	45.59	60.71
		28.36	48.32	62.52
		33.84	58.53	
		42.3	68.01	
		46.69	38.82	
		50.93	46.63	
		35.59	42.48	
		33.89	45.21	
			44.28	
			47.05	
			49.99	
			47.43	
			55.08	
			49.46	
			47.26	
Average	24.75222	39.2715	53.07741	78.76071
Stdev	6.568287	10.68626	11.78386	13.40969

Table 2: Detailed SEM data of P3HT thickness of various concentrations.

	Ag thickness /nm	20g/l P3HT on Ag thickness /nm		Ag thickness /nm	10gl P3HT on Ag thickness /nm
	83.2	122.7		104	136.3
	82.8	120.6		106.2	133.8
	79.4	121.1		102.7	137.8
	80.3	129.3		104.9	145.3
	80.6	125.7		103.8	137.3
	87	125.5		103.8	141
	91.3	132.4		103.2	132.4
	87.1	131.6		102.7	140.9
	88.9	124.7		100.8	133.4
	89.7	125.7		99.1	129.2
	88.5	123.5		98.3	116.5
	87.2	122.6		97.6	130.1
	87.4	129.1			129.1
	85.7	121.6			116.1
	87.2				
	85.7				
	85.9				
Average	85.759	125.44		102.26	132.8
Average thickness of P3HT/nm		39.68			30.541 66667
stdev/nm		4.01			8.44

Table 3. Detailed AFM data of P3HT thickness of various concentrations.